13B.6

APPLICATION OF AN IMMERSED BOUNDARY METHOD TO VARIATIONAL DOPPLER RADAR ANALYSIS SYSTEM

Sheng-Lun Tai[1], Yu-Chieng Liou[1], Juanzhen Sun[2], Shao-Fan Chang[1], Ching-Yu Yang[1]

[1]Department of Atmospheric Sciences, National Central University, Jhongli, Taiwan
[2]National Center for Atmospheric Research, Boulder, Colorado

1. Introduction

The Variational Doppler Radar Analysis System (VDRAS) has been widely used for nowcasting (Crook and Sun, 2002, 2004) and quantitative precipitation forecast (QPF) (Sun and Zhang, 2008). Although many successful applications by VDRAS were shown in recent years, the lack of ability to resolve terrain effect degrades its performance when encounter the environment with complex topography. Tai et al. (2011) merged VDRAS 4DVAR analysis field with WRF model field and forecast by WRF model. They demonstrated that positive impact can be achieved by resolving terrain using WRF.

In order to improve the analysis system, Ghost-cell Immersed Boundary Method (GCIBM) (Tseng and Ferziger, 2003) is applied to the analysis system. For the model verification, two idealized experiments are conducted, including a two-dimensional linear mountain wave simulation and a three-dimensional leeside vortex simulation. Furthermore, a real case forecast experiment is also demonstrated, which is initialized by no-terrain VDRAS 4DVAR analysis field. By comparing with model forecasting without terrain, the performance of modified model is evaluated.

2. The Variational Doppler Radar Analysis System (VDRAS)

The central process of VDRAS is the 4DVAR radar data assimilation, which includes a cloud-scale numerical model, the adjoint of the numerical model, a cost function, a minimization algorithm, and the specification of weighting coefficients. For details on each of these components, readers are referred to Sun and Crook (1997, 2001). The numerical model used to represent the convective-scale motion is anelastic, with Kessler-type warm rain microphysical parameterization.

There are six prognostic equations: the three velocity components (u, v, and w), the liquid water potential temperature (θl), the total water mixing ratio (qt), and the rainwater mixing ratio (qr). The pressure (p) is diagnosed through a Poisson equation.

Corresponding author address: Mr. Sheng-Lun Tai, Dept. of Atmospheric Sciences, National Central University, 320, Jhongli City, Taiwan; e-mail: taiolan430@gmail.com

The temperature (T) and the cloud water mixing ratio (q_c) are diagnosed from the prognostic variable.

3. Ghost-cell Immersed Boundary Method and the implementation

The immersed boundary method (IBM) has recently been demonstrated to be applicable to complex geometries in computational fluid dynamics (CFD). The Ghost-cell Immersed Boundary Method (GCIBM) is one variant of them and proposed by Tseng and Ferziger (2003), which can readily be implemented in any existing Cartesian grid code with staggered or non-staggered grids.

The “ghost-cell” is defined as the first grid point under the terrain surface. By giving the value that satisfies appropriate boundary conditions at every time step on those ghost cells, model implemented with GCIBM could simulate terrain effect reasonably well after integration. The numerical procedure for implementation of GCIBM is following:

(1) Detect the terrain boundary and determine the physical and ghost cell domains in the 3-D model domain (Fig. 1).
(2) Interpolate from points in physical domain to get the value on image point of ghost-cell (as I point in Fig. 1). And update ghost cell by imposing the boundary condition implicitly.
(3) Integrate the nonlinear model (only physical domain grid points) and solve the pressure Poisson equation to obtain the forecast at next time step.
(4) Update ghost-cell again by the new forecast field and certain boundary condition.

In this study, we impose Neumann boundary condition whereas ghost-cell equals image point for variables of horizontal winds, liquid water potential temperature perturbation and mixing ratios of total water, cloud water and rainwater. For vertical velocity, the ghost-cell equals boundary condition as

$$w = u\frac{dh_t}{dx} + v\frac{dh_t}{dy}, \qquad (1)$$

where h_t represents terrain height at each ghost-cell grid. By repeating steps 2 to 4 as the model integration continues, the expected results will be gradually obtained.

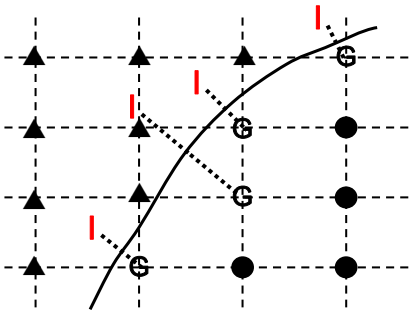

Fig. 1. Schematic of computational domain with an immersed boundary. ▲, point in the physical domain, G, point in the ghost cell domain and I, the image point of ghost cell. Dotted lines are perpendicular to the immersed boundary.

4. Verifications

4.1 2-D Linear Mountain Wave

Linear mountain waves are often simulated for comparisons with the available analytic solution. The behavior of linear mountain wave has been studied by previous research and is summarized by Smith (1980). If the upstream wind speed is uniform (no vertical shear), the behavior of linear hydrostatic mountain wave can be described by the following equation

$$\frac{\partial^2 \delta}{\partial z^2} + l^2 \delta = 0. \qquad (2)$$

If the atmosphere is isothermal, l (Scorer parameter) is constant,

$$l^2 = \frac{g}{c_p \bar{T} \bar{U}^2} - \frac{g^2}{4R^2 \bar{T}^2}. \qquad (3)$$

A bell-shaped mountain contour is specified as

$$z(x) = \frac{ha}{x^2 + a^2}, \qquad (4)$$

with an imposed linearized boundary condition $\delta(x,0) = z$ at the surface, and the radiation boundary condition for the upper boundary. The solution subject to these boundary conditions is

$$\delta(x,z) = \left(\frac{\rho_0}{\bar{\rho}}\right)^{1/2} ha \frac{a\cos lz - x \sin lz}{x^2 + a^2}. \qquad (5)$$

The analytical solution of perturbation horizontal and vertical velocities are calculated from these relation

$$u' = -\frac{\bar{U}}{\bar{\rho}} \frac{\partial \bar{\rho} \delta}{\partial x}, \quad w' = \bar{U} \frac{\partial \delta}{\partial x}. \qquad (6)$$

In this test, the parameters that satisfy the requirements are chosen as following: T = 250K, U = 20 ms^{-1}, a = 10 km, h = 1 m. The length of horizontal domain is 202 km with grid interval 2 km, and 20 km for domain height with constant vertical spacing as 0.2 km. The sponge layer is set at the upper half domain. Results from the analytical solution and model simulation obtained at $\bar{U}t/a$ = 60 for perturbation vertical velocity are displayed in Fig. 2. As evidenced in Fig. 2, the numerical and analytical solutions agree well in both wave length and magnitude.

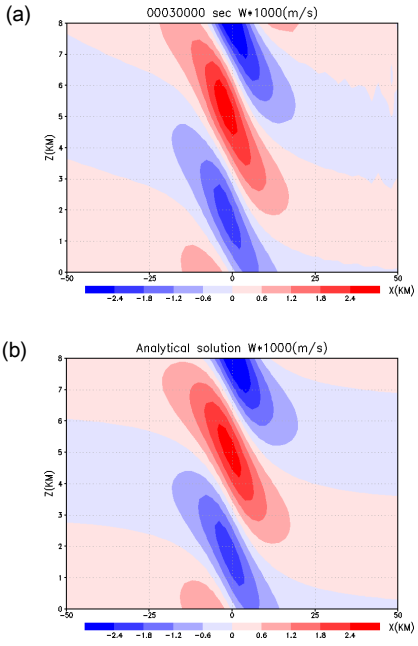

Fig. 2. The vertical velocity field of 2-D linear mountain wave. (a) Simulated result at 30000 seconds ($\bar{U}t/a$ = 60), (b) Analytical solution; both the magnitudes have been amplified by 1000.

4.2 3-D Lee-vortex Simulation

In addition to two-dimensional simulation, the three-dimensional lee-vortex simulation was also conducted for more examination. The model initialized with horizontal isentropic surfaces, corresponding to a uniform Brunt–Väisällä frequency of N = 0.01 s^{-1} and wind speed of U = 6 ms^{-1}. A bell-shaped mountain of 3 km height and half-width 10 km is located at left of domain center, and the distance from center is quarter of x-direction domain size. The horizontal domain has constant grid size of 2 km and contains 151 and 121 uniform grids in the x and y directions, respectively. In the vertical direction, there are 40 levels with interval of 0.25 km. In order to prevent reflection of vertical propagating gravity waves, sponge layers are employed in the upper portion of the model domain.

From the above related parameters, the Froude number (U/NH) equals 0.2, which is in the interval (under 0.5) that reversed flow and vortices are expected to appear in the low-level of lee side (Smolarkiewicz and Rotunno, 1989). It was also mentioned that the process occurs without viscosity-boundary layer.

The simulated result at $\bar{U}t/a$ = 7.2, as shown in Fig. 3a, is compatible with results at $\bar{U}t/a$ = 9 in Smolarkiewicz and Rotunno (1989) and $\bar{U}t/a$ = 5 by Schär and Durran (1997). As the time evolves, the lee vortices developed toward downstream and become elongated as shown in Fig. 3b. Since the shape and size of the

lee vortex are related to the advection scheme and intensity of numerical dissipation, exact comparison is not so meaningful. Overall, the simulated flow evolution is mostly consistent with previous studies.

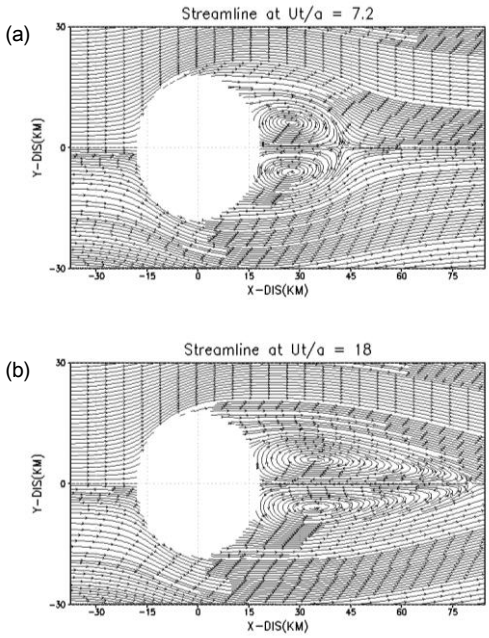

Fig. 3. 3-D lee vortex model simulation results at (a) Ut/a = 7.2 and (b) Ut/a = 18. The model height is at 0.375 km.

5. Real case simulation

Although the two verification simulations have shown the ability on simulating reasonable terrain effect, investigation is still needed when running in a real case with complex terrain and moisture. And since we focus on the improvement of the prediction performance, the test is designed to see the difference between model forecast with and without terrain.

For closer approaching to whole VDRAS system, both forecast experiments are initialized by a VDRAS 4DVAR analysis with dynamic, thermodynamic and microphysics variables. The case selected for assimilation is from IOP8 of South-West Monsoon Experiment (SoWMEX). The line convections developed in a Mei-Yu front passed through southwestern Taiwan, resulted in heavy rainfall especially on the windward (southwestern) side.

The assimilation strategy and following forecasts are depicted in Fig. 4. Basically, the assimilation procedure starts at 1022 UTC June 14 2008 and ends at 1102 UTC. During this period of time, two assimilation windows are included and also a forecast inserted in between. Three radars located at southwestern Taiwan (RCKT, RCCG and SPOL) are assimilated with background field prepared by radiosonde and surface mesonet station observations. After the assimilation procedure is accomplished, the analysis field is integrated by the full nonlinear model with (hereafter named IBMVDRAS) and without (VDRAS) terrain for two hours long.

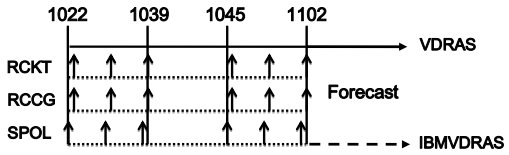

Fig. 4 Assimilation strategy and experiment designs for the real case simulation test. The first assimilation cycle is from 1022 UTC to 1039 UTC 14 2008 and 1045 UTC to 1102 for the second cycle. A period of forecast is arranged at between.

5.1 Comparison on forecast field

The initial field for both experiments is taken from the larger domain which was used to assimilate and analyze, with 121×121 grid points in horizontal and 40 levels for vertical direction. $\Delta x = \Delta y = 2$ km and $\Delta z = 0.35$ km.

From the calculated difference between two experiments, the southwestern flow is blocked by the southern part of Central Mountain Range (CMR) in Taiwan as evidence in increased pressure perturbation (Fig. 5a). The higher pressure located at windward side results distinct decrease of wind speed near mountain as shown in Fig. 5b. The wind flows along the terrain boundary near-mountain region is clear. By looking at convective cell's vertical structure (not shown), the terrain-forced flow lifting strengthening vertical velocity and increasing the rainwater mixing ratio.

For more examination on precipitation forecast, two-hour quantitative precipitation forecasts (QPF) by both experiments are verified by rain gauges on the ground. At first, we compute the rain rate RR for each horizontal grid point on the surface-nearest model layer as follows

$$RR = \frac{q_r(V_T - w)\rho_a}{\rho_w}, \qquad (7)$$

where q_r (kg kg^{-1}) is the rainwater mixing ratio; ρ_a and ρ_w (kg m^{-3}) represent the air and water densities, respectively; V_T (m s^{-1}) stands for the terminal velocity and w is vertical velocity. Since RR has the unit meters per second, it is converted to the rainfall amount (mm) for each model time step (ΔT) by

$$PRE = RR \times 1000 \times \Delta T. \qquad (8)$$

Fig. 6 displayed the two-hour accumulated rainfall amounts from rain gauge observation, VDRAS, IBMVDRAS and also the difference from both forecasts. The results reveal the terrain really affects the development of convective cells, which cause significant decrease in precipitation on the northern ridge of CMR as shown in Fig 6d. In the mean time, strengthened convective cells in windward side increase precipitation

significantly.

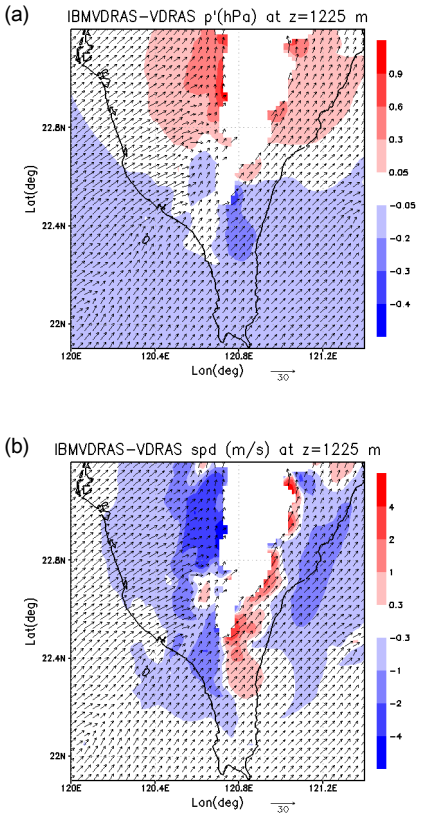

Fig. 5. The difference between IBMVDRAS and VDRAS (IBMVDRAS minus VDRAS) of (a) pressure perturbation (hPa) and (b) wind speed (ms^{-1}) after 1 hour simulation time, the level is at 1.225 km.

5.2 Verification on precipitation forecast

For the purposes of comparison, the predicted rainfall amounts distributed at the model grid points are interpolated to each rain gauge site (total 86 sites). Then, the equitable threat score (ETS) proposed by Schaefer (1990) is utilized to provide a quantitative comparison in QPF accuracy under different scenarios. This index is defined as

$$ETS = \frac{H - R}{F + O - H - R}, \qquad (9)$$

where H is the number of correctly predicted points above a certain threshold, F stands for the number of forecast points above a threshold, O represents the number of observed points above a threshold, and R is the number of hits by chance, which can be written as

$$R = \frac{F \times O}{N}, \qquad (10)$$

where N is the total number of points in the verification domain. When ETS = 1, it implies a perfect forecast.

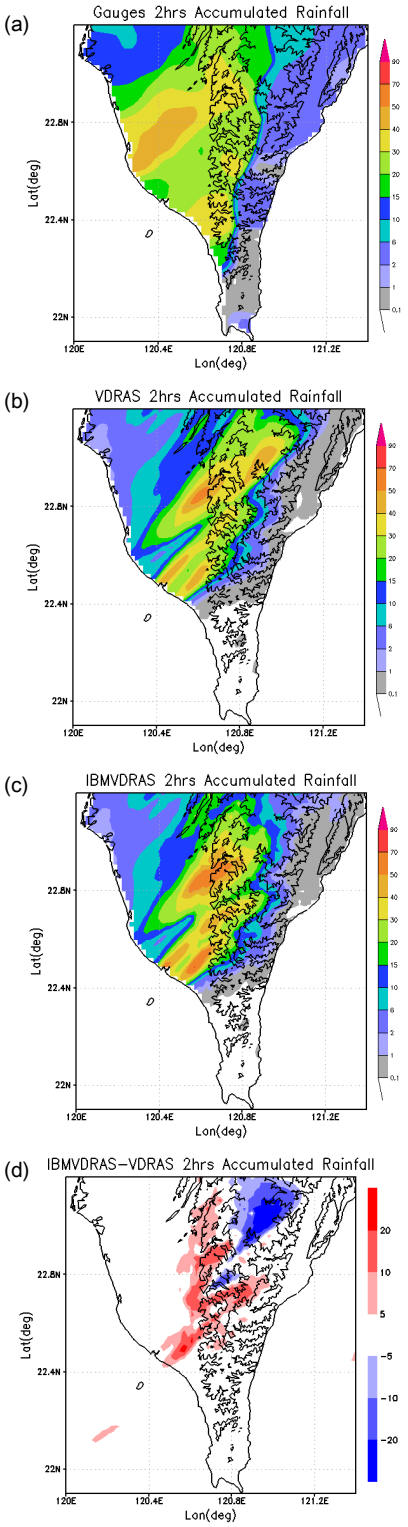

Fig. 6. 2 hours accumulated rainfall amount (mm) for: (a) Rain gauge observation, (b) VDRAS experiment and (c) IBMVDRAS experiment. (d) The difference between IBMVDRAS and VDRAS (IBMVDRAS minus VDRAS).

Fig. 7 shows the ETS for both VDRAS and IBMBVDRAS experiments. The IBMVDRAS obviously performs better than VDRAS in all thresholds (6, 10, 14, 18 and 22 mm). Thus, it is believed that adding terrain effect has positive

impact on the precipitation forecast. The satisfactory results from IBMVDRAS are encouraging, since the rain gauges distribution is much denser in plain than in mountainous area.

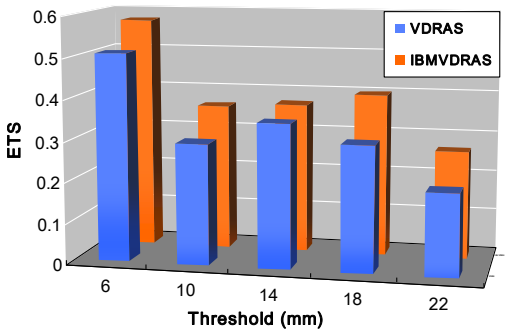

Fig. 7. The ETS calculated from 2 hour accumulated precipitation forecasts by VDRAS (blue bar) and IBMVDRAS (orange bar) experiments at different thresholds (6, 10, 14, 18 and 22 mm).

6. Summary

In this study, the terrain effect is implemented to VDRAS system using IBM method. The validation is accomplished by a two-dimensional linear mountain wave simulation, and the result agrees well with the analytical solution in both wave length and magnitude. Furthermore, a three-dimensional leeside vortex simulation is also conducted for more examination. The growth and development of a pair of symmetric vortices are compatible with previous research, which indicated that the terrain effect is well reproduced. Lastly, a real case forecast experiment is tested by performing model initialization and forecast using non-terrain VDRAS and IBMVDRAS, respectively. The terrain effect is obviously shown by dynamic variables and pressure perturbation in the forecast fields, leading to a clear improvement on QPF skill.

Since VDRAS is a 4DVAR analysis system, the adjoint model in the system should also be modified according to changes in the forward model. A more sophisticated analysis system is expected after the works on adjoint model are completed with the capability to resolve terrain.

ACKNOWLEDGEMENTS

This research is supported by Central Weather Bureau of Taiwan, under Grant MOTC-CWB-102-M-11.

REFERENCES

Crook, N. A., and J. Sun, 2002: Assimilating radar, surface, and profiler data for the Sydney 2000 forecast demonstration project, *J. Atmos. Oceanic. Technol.*, **19**, 888-898.

——, and ——, 2004: Analysis and Forecasting of the Low-Level Wind during the Sydney 2000 Forecast Demonstration Project. *Wea. Forecasting*, **19**, 151-167.

Schaefer, J. T., 1990: The critical success index as an indicator of warning skill. *Wea. Forecasting*, **5**, 570–575.

Schär, C. and Dale R. Durran, 1997: Vortex Formation and Vortex Shedding in Continuously Stratified Flows past Isolated Topography. *J. Atmos. Sci.*, **54**, 534–554.

Smith, R. B., 1980: Linear theory of stratified hydrostatic flow past an isolated mountain. *Tellus*, **32**, 348-364.

Smolarkiewicz, P. K., and R. Rotunno, 1989: Low Froude number flow past three-dimensional obstacles. Part I: Baroclinically generated lee vortices. *J. Atmos. Sci.*, **46**, 1154-1164.

Sun, J. and N. A. Crook, 1997: Dynamic and microphysical retrieval from Doppler radar observations using a cloud model and its adjoint. Part I: Model development and simulated data experiments. *J. Atmos. Sci.*, **54**, 1642–1661.

——, and ——, 2001: Real-time low-level wind and temperature analysis using single WSR-88D data. *Wea. Forecasting*, **16**, 117–132.

——, and Y. Zhang, 2008: Analysis and prediction of a squall line observed during IHOP using multiple WSR-88D observations. *Mon. Wea. Rev.*, **136**, 2364–2388.

Tai, S. L., Y. C. Liou, J. Sun, S. F. Chang, and M. C. Kuo, 2011: Precipitation Forecast using Doppler Radar Data, a Cloud Model with Adjoint, and the Weather Research and Forecasting Model – Real Case Studies during SoWMEX in Taiwan, *Wea. Forecasting*, **26**, 975-992.

Tseng, Y. and J. Ferziger, 2003: A ghost-cell immersed boundary method for flow in complex geometry. *J. Comput. Phys.*, **192**, 593–623.